Pacific Northwest
NATIONAL LABORATORY

PNNL-33428, Rev 0
DVZ-RPT-085, Rev 0

Geophysical Characterization and Monitoring of the 200 Area Treated Effluent Disposal Facility to Support Permit Renewal

TEDF Geophysical Monitoring

September 2022

Tim Johnson
Jon Thomle
Kelsey Peta
Jack Cambeiro

U.S. DEPARTMENT OF ENERGY

Prepared for the U.S. Department of Energy
under Contract DE-AC05-76RL01830

DISCLAIMER

This report was prepared as an account of work sponsored by an agency of the United States Government. Neither the United States Government nor any agency thereof, nor Battelle Memorial Institute, nor any of their employees, makes **any warranty, express or implied, or assumes any legal liability or responsibility for the accuracy, completeness, or usefulness of any information, apparatus, product, or process disclosed, or represents that its use would not infringe privately owned rights**. Reference herein to any specific commercial product, process, or service by trade name, trademark, manufacturer, or otherwise does not necessarily constitute or imply its endorsement, recommendation, or favoring by the United States Government or any agency thereof, or Battelle Memorial Institute. The views and opinions of authors expressed herein do not necessarily state or reflect those of the United States Government or any agency thereof.

PACIFIC NORTHWEST NATIONAL LABORATORY
operated by
BATTELLE
for the
UNITED STATES DEPARTMENT OF ENERGY
under Contract DE-AC05-76RL01830

Printed in the United States of America

Available to DOE and DOE contractors from the
Office of Scientific and Technical Information,
P.O. Box 62, Oak Ridge, TN 37831-0062;
ph: (865) 576-8401
fax: (865) 576-5728
email: reports@adonis.osti.gov

Available to the public from the National Technical Information Service
5301 Shawnee Rd., Alexandria, VA 22312
ph: (800) 553-NTIS (6847)
email: orders@ntis.gov <https://www.ntis.gov/about>
Online ordering: http://www.ntis.gov

PNNL-33428, Rev 0
DVZ-RPT-085, Rev 0

Geophysical Characterization and Monitoring of the 200 Area Treated Effluent Disposal Facility to Support Permit Renewal

TEDF Geophysical Monitoring

September 2022

Tim Johnson
Jon Thomle
Kelsey Peta
Jack Cambeiro

Prepared for
the U.S. Department of Energy
under Contract DE-AC05-76RL01830

Pacific Northwest National Laboratory
Richland, Washington 99354

Executive Summary

The Treated Effluent Disposal Facility (TEDF), located in the 200 East Area of the Hanford Site, is a site where non-hazardous and non-radioactive liquid wastes are disposed into two state-permitted infiltration basins. In 2016, the Washington State Department of Ecology denied a permit renewal request for TEDF due to the inability to adequately assess the impact of TEDF discharge water on the underlying groundwater quality. TEDF overlies the relatively impermeable Ringold Lower Mud (RLM) unit, whose upper contact lies in the vadose zone approximately 30 m below ground surface and approximately 10 m above the water table boundary. The RLM is assumed to isolate TEDF discharge water from the natural groundwater aquifer, which is monitored using wellbores screened below the RLM. Therefore, samples collected from monitoring wells near TEDF are not considered representative of TEDF discharge water. Rather, TEDF discharge water is assumed to mound on top of the RLM to form a perched aquifer.

To support permitting of the TEDF, a new monitoring well is required that can be used to sample water from the presumed perched water aquifer above the RLM. Ideally, the screened section of the well would be located at the peak of the perched water mound(s), which presumably occurs at the point of maximum vertical flux from TEDF to the RLM, or equivalently where the dominant infiltration flow paths reach the RLM. This report describes how time-lapse 3D electrical resistivity tomography (ERT) was used in conjunction with nominal TEDF discharge operations to image the dominant flow paths from each pond to the RLM.

Results are summarized in Figure ES.1. Figure ES.1A shows a satellite image of the TEDF overlain by an array of surface ERT electrodes. The solid and dashed black circles denote the zones of maximum vertical flux at the RLM within the south and north ponds, respectively, and presumably the regions where perched water peaks during discharge. Figure ES.1B shows time-lapse difference imaging results approximately 15 days after switching discharge from the south pond to the north pond. Blue iso-surfaces beneath the north pond denote regions of increasing bulk electrical conductivity caused by increasing saturation due to infiltrating water. Red iso-surfaces beneath the south pond denote regions that were previously saturated during the south pond discharge and are now de-saturating, causing a decrease in bulk electrical conductivity. In both cases, the zones of maximum change mark the dominant flow paths to the RLM. Figure ES.1C shows time-lapse imaging results approximately 15 days after switching discharge from the north pond to the south pond. In this case, blue iso-surfaces mark the dominant flow paths to the RLM from the south pond. The red iso-surfaces mark the dominant flow paths that existed during discharge to the north pond. The regions of maximum change in bulk conductivity (due to saturation or desaturation) that mark the primary flow paths are equivalent in both cases and denoted by the dashed solid and black circles. If a perched water zone forms on the RLM, it is likely to mound within or near the dashed circle during discharge to the north pond, and in the solid circle during discharge to the south pond. In other words, if perched water mounding occurs, the circles mark the optimum locations suggested by the ERT imaging for monitoring boreholes to be placed, enabling samples to be collected that are representative of TEDF discharge impacts on groundwater quality.

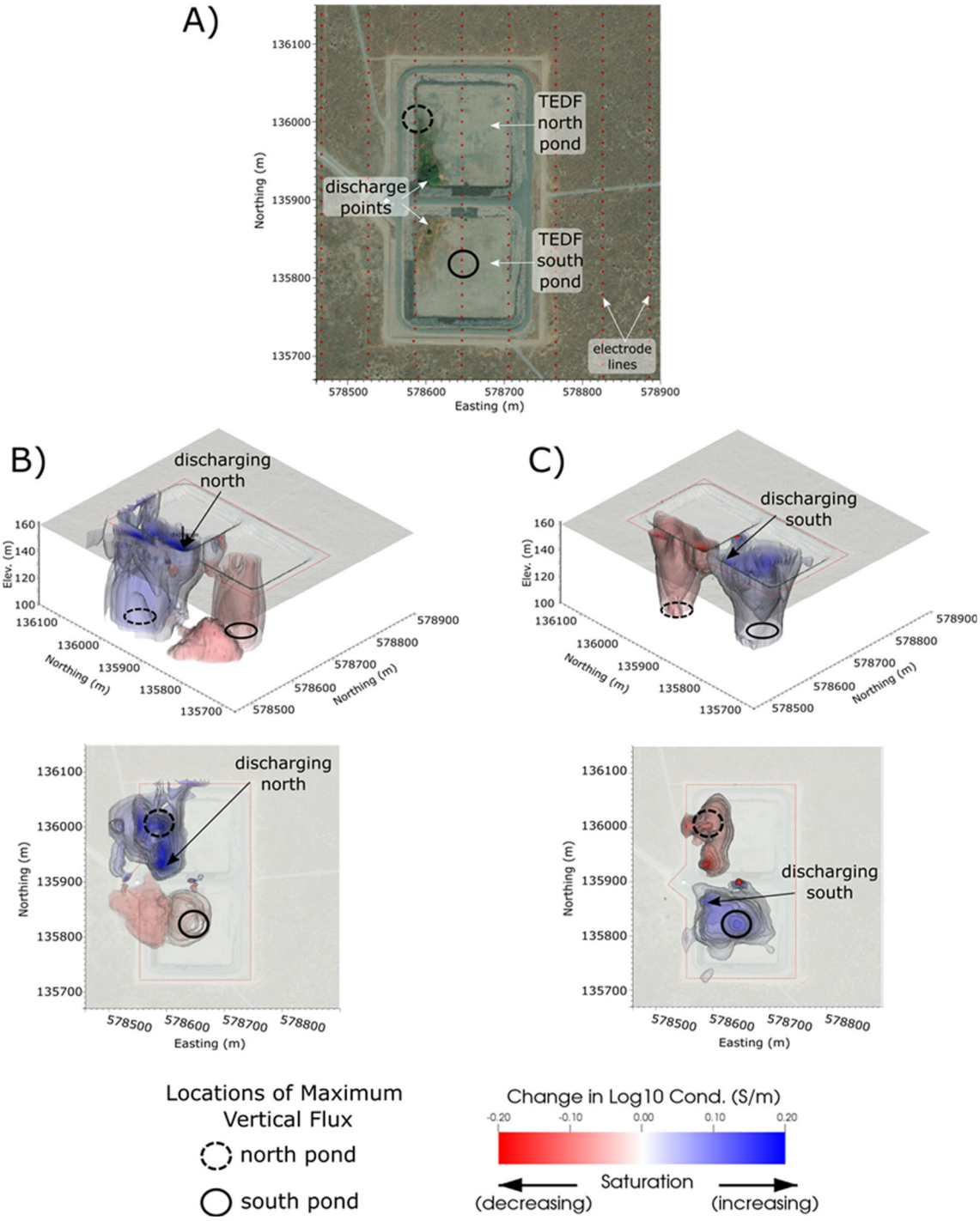

Figure ES.1. A) Satellite view of TEDF and surface electrode locations used in the time-lapse imaging. B) 3D time-lapse ERT difference image taken approximately 15 days after discharge was switched from the south pond to the north pond. C) 3D time-lapse ERT image taken approximately 15 days after discharge was switched from the north pond to the south pond. The dashed and solid circles denote the zones of maximum flux to the RLM indicated by the time-lapse ERT imaging.

Acknowledgments

Funding for this work was provided by the U.S. Department of Energy Richland Operations Office under the Deep Vadose Zone – Applied Field Research Initiative. The Pacific Northwest National Laboratory is operated by Battelle Memorial Institute for the Department of Energy under Contract DE-AC05-76RL01830.

Acronyms and Abbreviations

BEC	bulk electrical conductivity
ERT	electrical resistivity tomography
RLM	Ringold Lower Mud
TEDF	Treated Effluent Disposal Facility

Contents

Figures

Tables

1.0 Introduction

The Treated Effluent Disposal Facility (TEDF) is a site where treated non-hazardous and non-radioactive liquid wastes are collected and disposed to two state-permitted disposal basins within the 200 East Area at the Hanford Site. In 2016, a renewal application was submitted for TEDF that requested mass loading effluent limits instead of concentration-based effluent limits (WRPS-1602336, 2016). The Washington State Department of Ecology denied this request due to a lack of groundwater monitoring wells that can be used to identify and characterize the impact of TEDF discharges to the underlying groundwater. Current TEDF monitoring wells are in the confined aquifer below the Ringold Lower Mud (RLM) unit and are not considered representative of TEDF discharges that may mound above the RLM unit (Figure 1) to form a perched water aquifer.

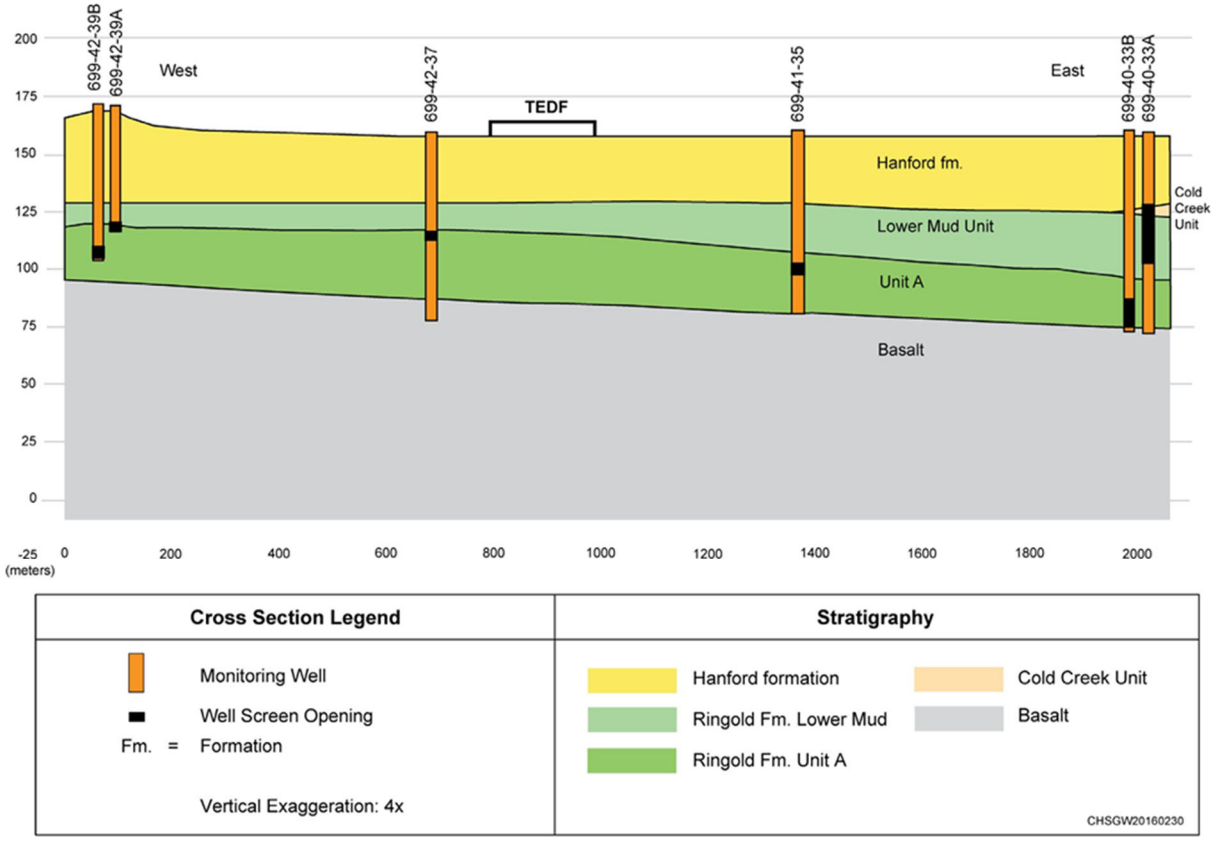

Figure 1. West-east cross section showing stratigraphy beneath the TEDF. The water table occurs at approximately 120 m in elevation. The upper contact of the Ringold Lower Mud unit occurs at approximately 130 m in elevation. (Source: WRPS-1602336, 2016)

To assess the impact of TEDF discharge on groundwater, there is a need to install a monitoring well that can be used to collect a representative sample of TEDF discharge water from above the RLM unit. Ideally, the screened zone of the well would be placed at the peak of the perched water mound to ensure a saturated water column sufficiently deep for sampling. Electrical resistivity tomography (ERT) was identified as a potential method of informing optimal well placement by (1) imaging important stratigraphic features influencing discharge water migration pathways and/or (2) directly imaging the dominant migration pathways to the RLM, and presumably to the peak of the perched water mound, using time-lapse ERT imaging.

A numerical modeling assessment was undertaken to investigate the performance of ERT for identifying a suitable location for a new sampling well. Results of that feasibility evaluation study provided the basis to install a surface ERT array over TEDF, and to monitor TEDF discharges long enough to identify the primary flow pathways through the vadose zone to the RLM unit. To identify primary flow pathways, a surface array consisting of 8 lines with 32 electrodes per line was installed within and adjacent to the ponds. The array collected data from January through August of 2022. After baseline ERT data were collected in January, TEDF discharge rates were increased to reproduce the high-flow conditions simulated in the performance assessment. Unfortunately, ERT data collected during high-flow conditions were inadequate to monitor associated hydrologic responses due to damaged field instrumentation. Once those equipment issues were addressed, long-term ERT monitoring commenced from March through August 2022, with approximately 12 ERT surveys collected per day under nominal, low-flow discharge conditions. ERT data collected during this period revealed that discharges were switched between the north and south ponds monthly from March through June. The resultant changes in saturation (i.e., increasing beneath the current discharge pond and decreasing beneath the previous discharge pond) provided sufficient contrast in bulk electrical conductivity (BEC) to identify dominant flow paths through the vadose zone to the RLM. Assuming perched water thickness is largest where infiltration flow paths meet the perched water table, the flow paths can be used to inform candidate locations for the new sampling well. The remainder of this report describes (1) the assumptions and results of the ERT feasibility and performance assessment and (2) the ERT field array installation, operation, data analysis, and results.

2.0 Pre-deployment ERT Performance Assessment

Numerical ERT performance modeling was conducted based on MODFLOW-simulated TEDF discharges and resultant unsaturated flow provided by CPCC-00327, Rev. 0. Figure 2 shows the discretized TEDF basins and assumptions used in the MODFLOW simulation. Discharges were assumed to occur concurrently in the north and south ponds, with areas of water ponding during normal and high discharge rates shown in blue and green, respectively.

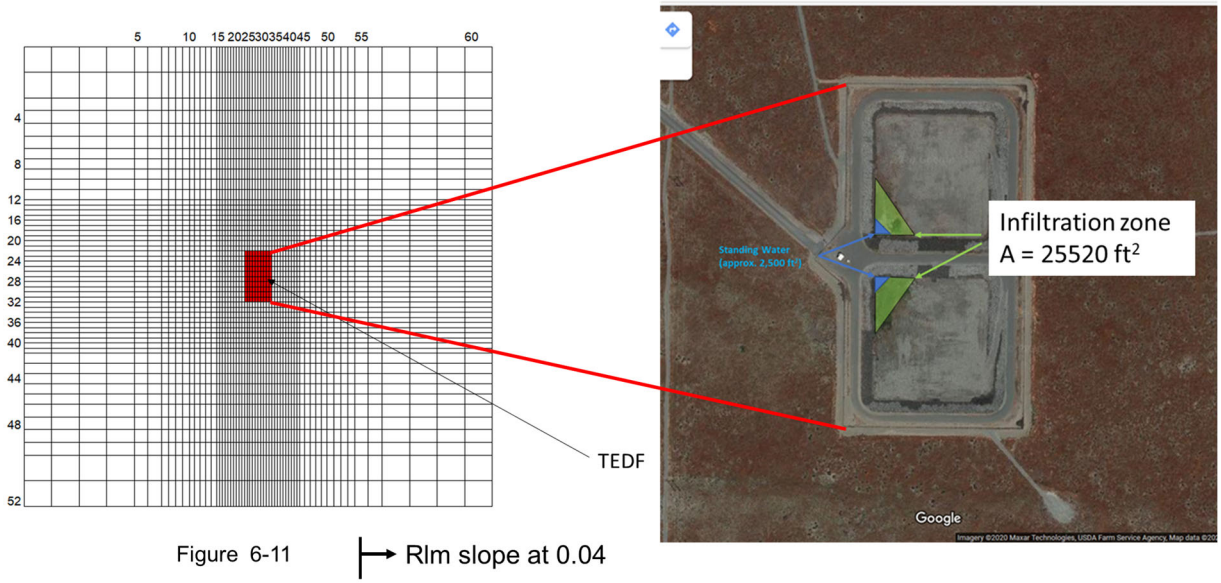

Figure 2. Discretized model (left) of TEDF (right). The north and south basins slope downward toward the discharge points (shown in blue). The blue and green areas represent the assumed ponding zones during normal flow and high flow, respectively (CPCC-00327, 2021).

Figure 3 shows the simulated discharge rate for the time period considered in the ERT performance assessment. From time zero to 243 days, constant infiltration was simulated through the blue areas in Figure 2 at a rate of 11,500 ft^3/d, which established steady state flow conditions. At day 243, the infiltration rate was increased to 197,000 ft^3/d through the green areas shown in Figure 2 and was held at that rate for 30 days before returning to the baseline flowrate.

The increase in flowrate at day 243 causes an increase in vadose zone saturation, and a corresponding increase in BEC that serves as the target for time-lapse ERT imaging. A baseline ERT image was simulated just before the flowrate increase. Subsequent time-lapse ERT images were then simulated during the high-flow period and differenced from the baseline image to reveal the change in vadose zone BEC caused by the increase in saturation.

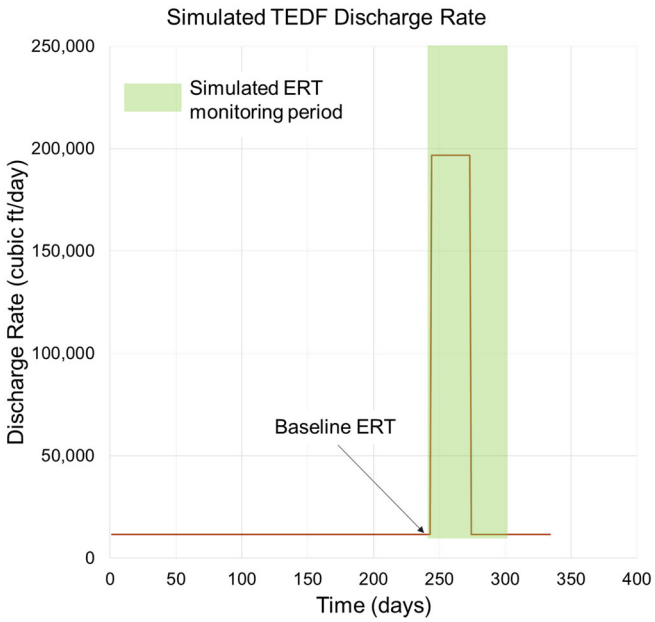

Figure 3. Simulated discharge rate.

A flow diagram of the performance modeling is shown in Figure 4. First, the MODFLOW simulation produces grid-discretized 3D saturation vs. time. Saturation distributions at each time-step are then interpolated to the ERT simulation mesh. Using Archie's law,

$$BEC = \sigma_w \phi^m S^n, \quad (1)$$

where σ_w represents pore fluid conductivity, ϕ represents porosity, S represents saturation, m represents the cementation coefficient, and n represents the saturation coefficient. Using the assumed Archie's parameters listed in Table 1, the mesh-discretized porosity and saturation were converted to BEC at each time step. These BEC distributions served as the true values by which the corresponding ERT images were evaluated.

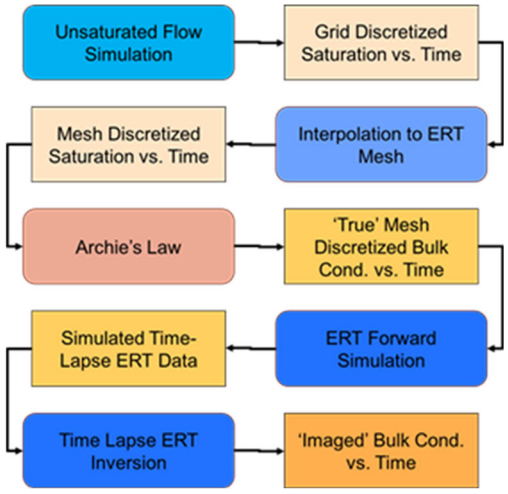

Figure 4. Flow diagram for numerical ERT imaging based on MODFLOW simulation of TEDF discharge. ERT imaging performance was assessed by visually comparing the "true" BEC vs. time to the "imaged" BEC vs. time.

Table 1. Archie's law parameters used to convert MODFLOW output to BEC.

Parameter	Value
Groundwater conductivity (σ_w)	0.015 S/m
Vadose zone and discharge water conductivity (σ_w)	0.040 S/m
Cementation exponent (m)	1.3
Saturation exponent (n)	2.0
Saturation (S)	Extracted from MODFLOW simulation
Porosity (ϕ)	Extracted from MODFLOW simulation

Next, using the surface electrode array shown in Figure 5, ERT survey data were simulated for each time step to produce the field ERT data under the given assumptions. Finally, random noise characteristic of anticipated field conditions (5% of the absolute value of the measurements) was added to each ERT data set prior to inversion. The noisy data were then inverted and the resulting ERT images were visually compared to the true BEC distributions to assess imaging performance.

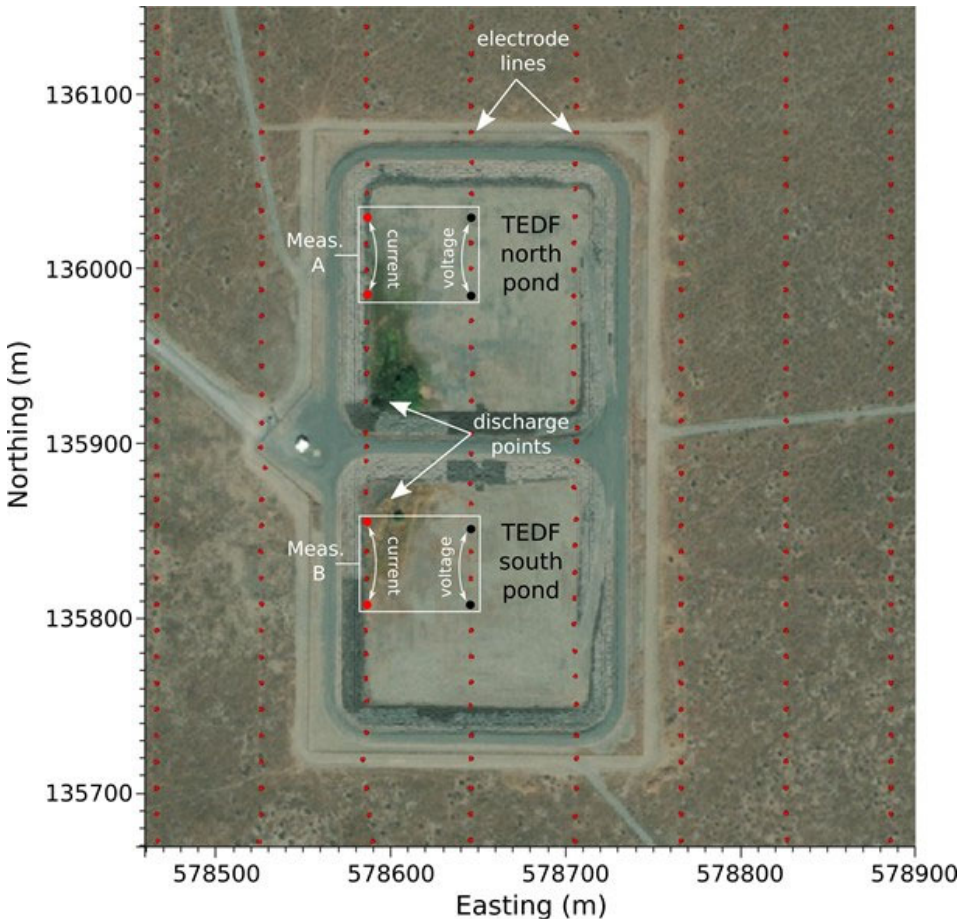

Figure 5. Satellite image of TEDF with superimposed electrode locations used in both the feasibility simulations and the field deployment. ERT data time-series for measurements A and B are shown in Figure 8 to illustrate the effects on raw ERT data of separate discharge to the north and south ponds.

A summary of the ERT performance assessment is shown in Figure 6, including the baseline image taken after 243 days of infiltration at 11,500 ft^3/d; time-lapse difference images at 1, 12, and 30 days after the start of infiltration at 197,000 ft^3/d; and a time-lapse difference image taken 9 days after the return to the baseline infiltration of 11,500 ft^3/d. In each case, the time-lapse difference images show the change in BEC from the baseline image. Because the only parameter in Archie's law [Eq. (1)] that changes over time is saturation (S), the timing and location of changes in BEC are caused by corresponding changes in saturation. That is, the change in BEC over time serves as a proxy for change in saturation.

Figure 6A shows the actual and imaged baseline BEC. The elevated conductivity zone in the center of the image is caused by the elevated saturation beneath the ponds at baseline flow. Comparison of the actual versus imaged vadose zone BEC suggests that ERT can capture the 3D footprint of the infiltration zone, albeit at reduced resolution. For example, the transition from the unsaturated zone to the saturated zone at (x=1500 m, y=1500) is relatively sharp in the actual BEC and appears to be mounded in the imaged BEC. In addition, the magnitude of BEC is generally muted in comparison to the actual BEC, which is another effect of limited resolution (Day-Lewis et al., 2005). In general, the comparison of the actual and imaged BEC gives a realistic representation of the effects of limited resolution and should be considered when interpreting the baseline images derived from actual field data.

The time-lapse images in Figure 6B through E are shown in plan and oblique views. In plan view, changes in BEC are shown as iso-surfaces; in oblique view, they are shown in cross-section. Although the effects of limited resolution are evident, the footprint of the zone of increasing saturation captures the actual footprint well enough to locate the dominant flow paths to the vadose zone, which occur directly under ponding areas in this case. Vertical resolution at the depth of the water table is not sufficient to delineate the water table boundary (see oblique time-lapse difference cross sections in Figure 6). Because there is no clear evidence of perched water mounding in the actual BEC, it is unclear whether vertical resolution is sufficient to capture mounding in the time-lapse images for the synthetic case. As will be shown, there is evidence of mounding on the RLM in the time-lapse images derived from the field data. However, since the performance assessment does not clearly indicate that perched water mounding is resolvable, assessment of the field results is focused on the dominant flow paths to the RLM in terms of saturation, which is presumably where mounding would be highest.

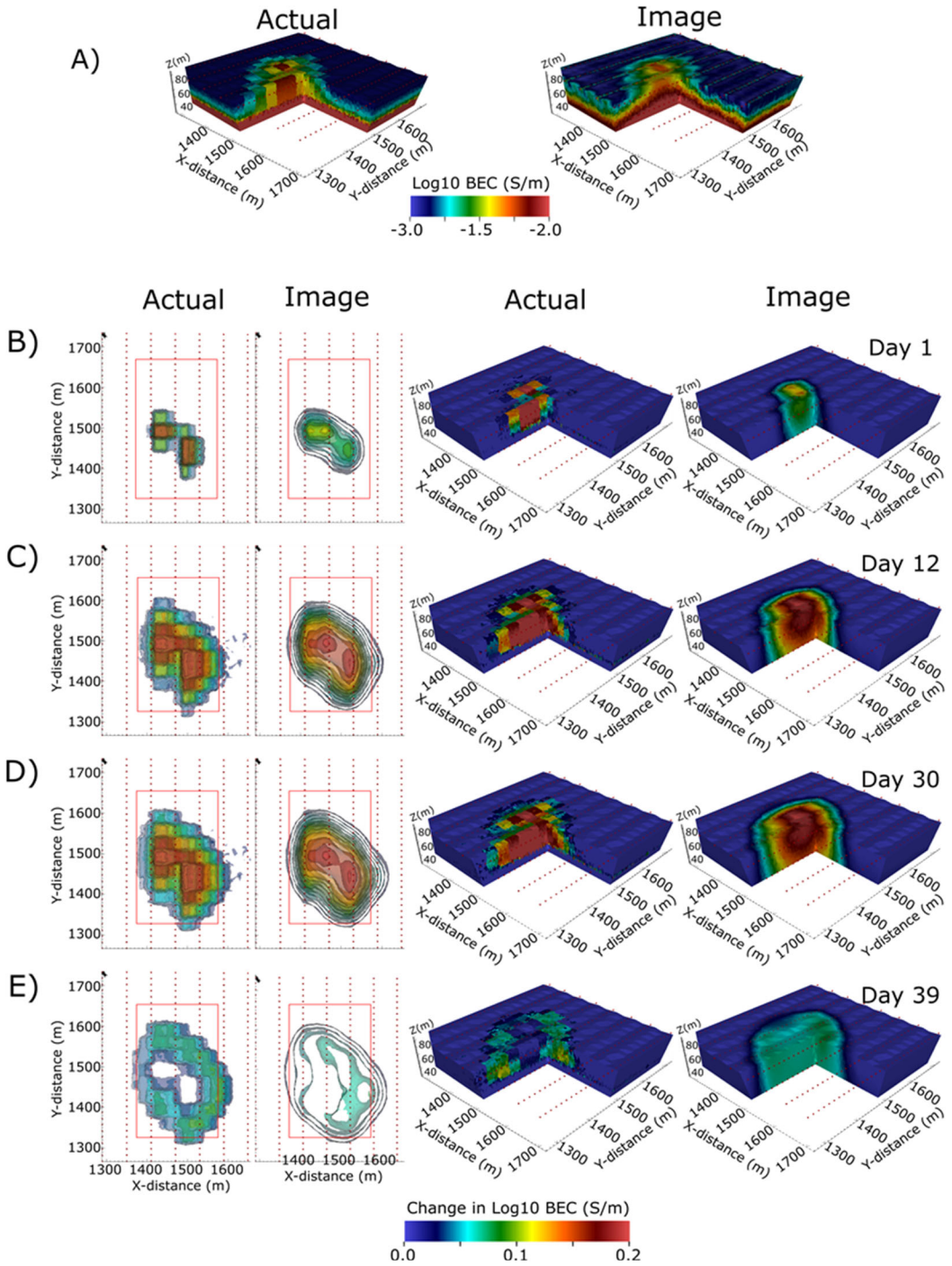

Figure 6. Summary results of ERT performance simulations. A) Actual and imaged baseline BEC after 243 day of infiltration at 11,500 ft^3/d. B, C, D) Actual and imaged changes in BEC from baseline after 1, 12, and 30 days of infiltration at 197,000 ft^3/d. E) Actual and imaged changes in BEC from baseline after 30 days of infiltration at 197,000 ft^3/d followed by 9 days of infiltration at 11,500 ft^3/d.

In summary, the feasibility assessment suggested that the ERT would not be able resolve the depth perched water mounding that may occur on the RLM during TEDF discharge. However, time-lapse difference ERT imaging would be able to locate the dominant flow paths to the RLM under high-flow conditions, using low-flow conditions as the baseline. These locations are presumably where maximum perched water mounding would occur and therefore where wellbores could be placed to increase the probability of encountering a saturated water column deep enough to collect representative samples. These conclusions are somewhat conservative because the simulations only considered changes in saturation caused by changes in TEDF discharge rates, and not changes in pore fluid conductivity, which may have increased the BEC contrast and improved the ERT imaging.

As will be shown, field ERT data collected during the high-discharge event that was monitored at TEDF was affected by damaged hardware (cables faulty and/or damaged by wildlife), making the data inadequate for effective time-lapse imaging. In addition, in comparison to the baseline discharge rates simulated in the feasibility study, actual discharge rates exhibited significant variability over relevant time scales (hours to days). Variable baseline discharge clearly caused variability in vadose zone saturation that influenced the ERT data, making the determination of a steady-state baseline BEC challenging. Fortunately, from March to June, discharges occurred only to either the north pond or the south pond, with monthly changes between the two. Changes in saturation beneath the ponds (i.e., desaturating in the “off” months and re-saturating in the “on” months) provided enough contrast in BEC to identify the dominant flow paths from each pond to the RLM.

3.0 Field-Scale ERT Monitoring

3.1 ERT Data Collection

Based on the ERT performance assessment, time-lapse ERT imaging was deemed to have an acceptable probability of locating the primary flow paths from the TEDF ponds to the RLM. Consequently, a surface ERT array identical to that shown in Figure 5 was installed over the TEDF ponds in early January of 2022.

Autonomous ERT data collection began in late January 2022, including 12 ERT surveys per day (once every 2 hours). Each survey consisted of a series of 5056 inline and crossline dipole-dipole measurements, optimized for time-resolution using an eight-channel data collection system (i.e., eight potential measurements were collected per current injection). Data collected from January through the end of February experienced a degradation in quality due to faulty ERT cables and/or cables being damaged by wildlife. The data collection during this time period was deemed unusable for the objectives in this work. Data collection stopped for a brief period and then resumed on February 20 after cables were repaired or replaced.

For reference, Figure 7 shows the TEDF discharge rate from December 30, 2021, through March 10, 2022. On February 14, a high-flow event was initiated to provide a saturation contrast target for time-lapse ERT imaging, like what was simulated in the feasibility assessment. As noted, the ERT data collected during this period were not useful until faulty cables were replaced on February 20. Consequently, useable baseline data were not collected prior to the high-flow event, making time-lapse imaging impossible. Electrodes and cables continued to experience disturbances from wildlife, resulting in ERT data of variable quality throughout the month of March. Analysis in this report focuses on data collected in March, April, and May of 2020. The time-series of every measurement for that period was manually inspected to identify and remove faulty measurements. After filtering, 2808 of the 5056 measurements were used for the time-lapse imaging.

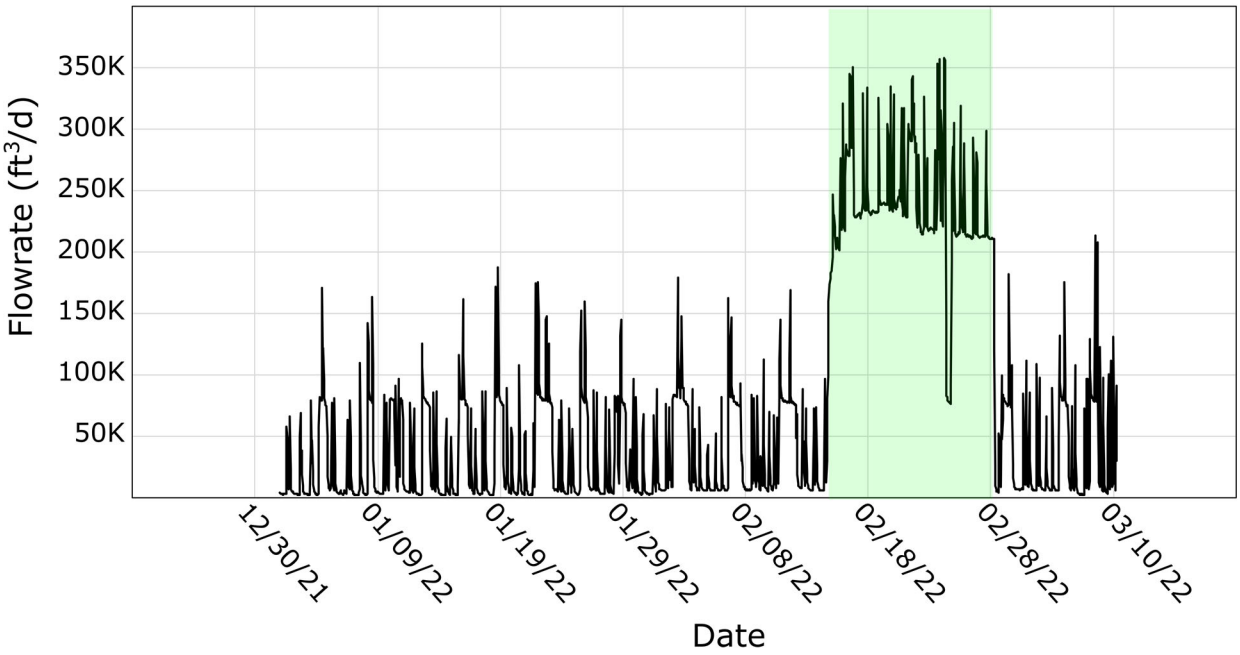

Figure 7. TEDF discharge rate showing variable baseline flow from 1/01/22 through 2/14/22 and high (but variable) flowrate from 2/14/22 through 2/28/22 applied to create a target for time-lapse difference imaging.

3.2 Difference ERT Imaging Strategy

In this report, baseline discharge refers to the discharge TEDF received under nominal conditions, as shown in Figure 7, from February 1 through 14. The variable nature of baseline discharge prohibits saturation from reaching a steady state condition and has significant influence on those ERT measurements that are sensitive to the ponding and infiltration zones. This characteristic was used to identify which pond was actively receiving discharge water from March 1 to June 1 and formed the basis for the time-lapse imaging strategy used in lieu of the high-discharge imaging. To illustrate, Figure 8 shows time-series of the two ERT measurements shown in Figure 5 in comparison to the total discharge rate. Each measurement is collected by injecting current between the current electrodes and measuring the corresponding electrical potential (or voltage) across the voltage electrodes. The raw measurement is the voltage normalized by the current. Measurement 1 is generally sensitive to BEC north of the discharge point in the north pond, and measurement 2 is generally sensitive to BEC south of the discharge point in the south pond. Figure 8C shows the total discharge rate without indicating which pond was receiving water.

During the months of March and May, measurement A was relatively stable but displayed relatively high variability in April. Measurement B displayed the opposite behavior, being relatively variable in March and May, and relatively stable in April. Assuming the high-variability periods in each measurement are caused by variability in discharge, it is possible to determine which pond is actively receiving water. Measurement A experiences high variability when the north pond is receiving discharge water and vice versa. Measurement B experiences high variability when the south pond is receiving water.

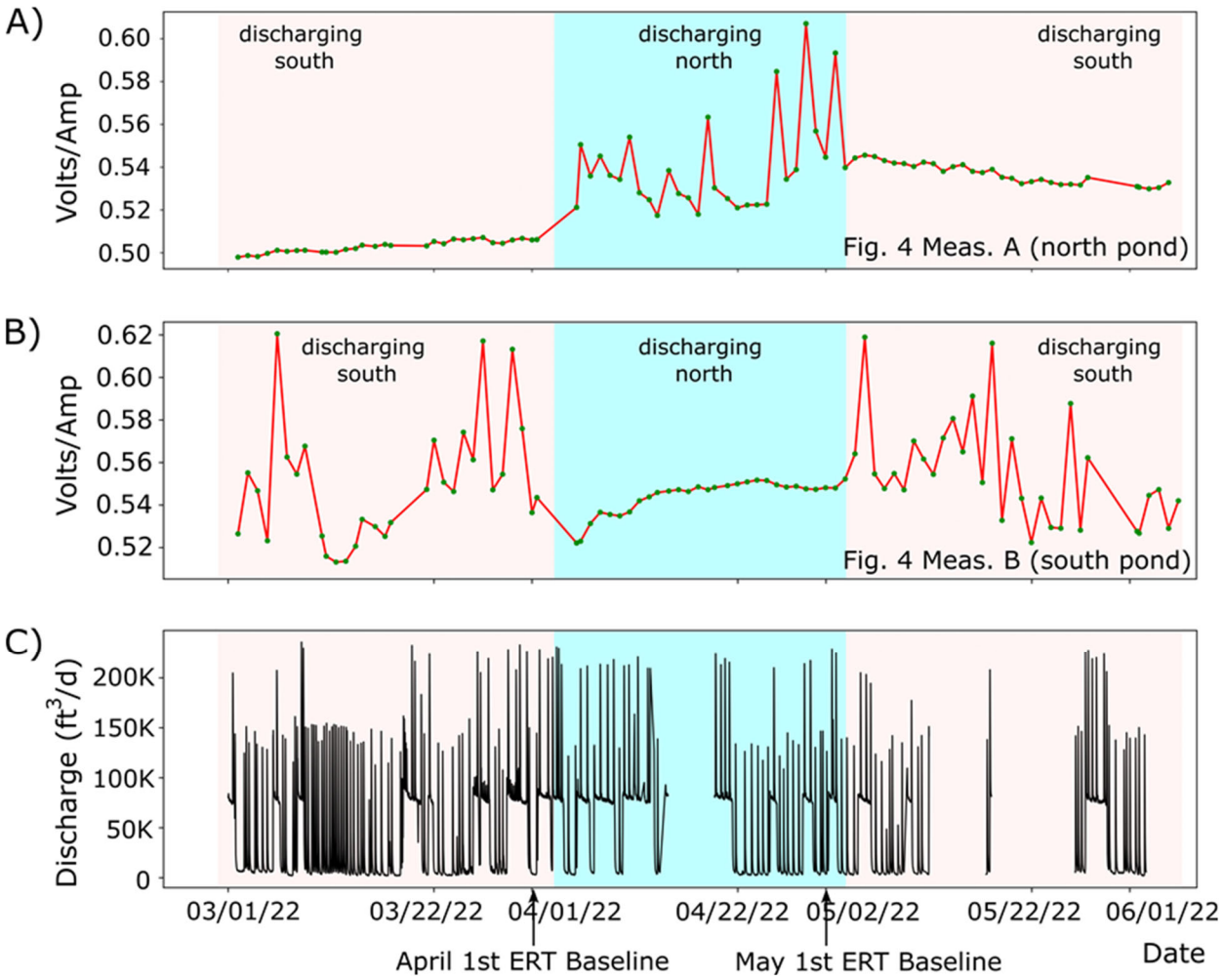

Figure 8. Example raw data time-series compared to TEDF discharge from March to June 2022. A) ERT raw data time-series for measurement A in Figure 5. B) ERT raw data time-series for measurement B in Figure 5. C) TEDF discharge rate.

The apparent switching of discharge between the north and south ponds from March through May provides the technical basis for the time-lapse imaging strategy presented in the forthcoming text. For example, at the end of March (i.e., April 1st Baseline in Figure 8C), the dominant flow paths from the south pond to the RLM are expected to be at relatively high saturation because the south pond has been receiving water for at least 30 days. Conversely, the dominant flow paths in the north pond are expected to be at relatively low saturation because the north pond has not received water for at least 30 days. Using the April 1 baseline condition for time-lapse imaging in April (when discharge is switched from the south pond to the north pond), the south pond will experience desaturation, *particularly along the dominant south-pond flow paths,* and the north pond will experience re-saturation, *particularly along the dominant north-pond flow paths*. Then, compared to the April 1 condition (Figure 8C), *decreases in BEC are expected along the dominant flow paths in the south pond*, and *increases in BEC are expected along the dominant flow paths in the north pond* during the north pond discharge period in April. Similarly, compared to the May 1 condition (Figure 8C), *increases in BEC are expected along the dominant flow paths in the south pond*, and *increases are in BEC are expected along the dominant flow paths in the north pond* during the south pond discharge period in May.

Given the expected saturation/BEC behaviors described above, the analysis proceeded with two time-lapse inversions using different baseline datasets. The first produces changes in BEC over the month of April from the April 1 baseline condition. The second produced changes in BEC over the month of May from the May 1 baseline condition. Dominant flow paths to the RLM beneath the north pond will be marked by the regions of largest increase and decrease in BEC in the first and second inversions, respectively. Conversely, dominant flow paths in the south pond will be marked by the regions of largest decrease and increase in BEC in the first and second inversions, respectively.

3.3 Sensitivity Analysis and Data Fit

A quality assessment of the ERT data time-series identified removal of ~44% of the measurements, leaving 2808 out of 5056 measurements for the time-lapse analysis. Although this represents an unusually large number of low-quality data, most of the measurements were from electrodes that were isolated to three areas. Namely, the eastern-most line, the northern half of the line at 578705 m easting, and the northern three electrodes of the line at 578525 all produced unusable data. To assess the effects of the data reduction, Figure 9 shows a map of the sensitivity of the data to each region of the subsurface in a series of depth sections. In a general sense, regions of high sensitivity equate to regions of higher imaging resolution.

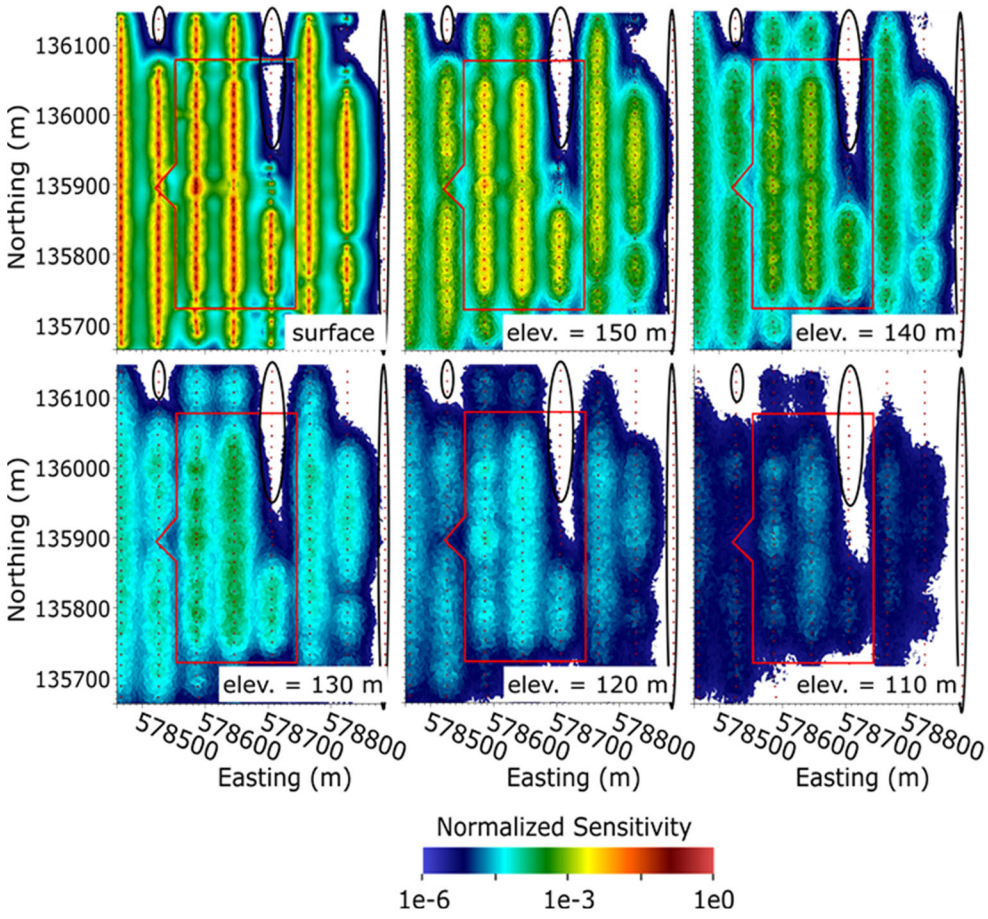

Figure 9. Normalized sensitivity of ERT data to the surface and subsurface at five different depths. Note the upper RLM contact is located at approximately 130 m in elevation. Poorly performing electrodes are circle in black.

As shown in Figure 9, the 2808 measurements used in the inversions have no sensitivity to the regions near the poorly performing electrodes. Figure 9 also shows a reduction in sensitivity with distance from the electrodes, indicating a reduction in resolution with depth. The regions of low sensitivity are not located where changes in saturation occur, and so have little effect on the time-lapse images.

One measure of overall data quality is the degree to which an inversion can find a reasonable BEC distribution that matches the observed ERT data. Figure 10 shows the simulated vs. observed ERT data for the April 1 baseline inversion, resulting in a coefficient of determination (R^2) of 99.45.

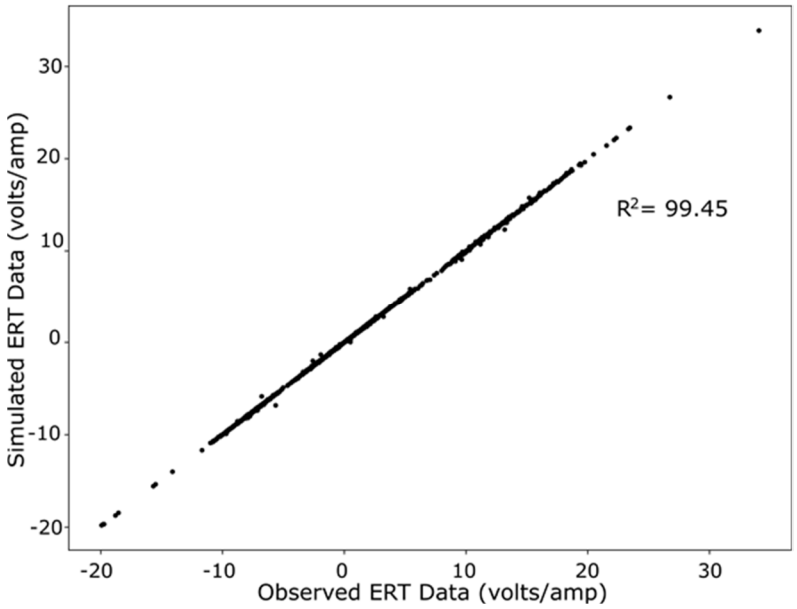

Figure 10. Observed vs. simulated ERT measurements for the April 1 baseline inversion (see Figure 8C).

Each ERT datum *i* was weighted with a standard deviation (sd_i) of

$$sd_i = 0.1abs(V_{obs,i}) + 0.01, \quad (2)$$

where $V_{obs,i}$ is the value of the measurement *i*. With this weighting, the April 1 baseline inversion was fit to a χ^2 value of 0.2, where

$$\chi^2 = 1/N\left(\sum_{i=1}^{N}\left(\frac{(V_{sim,i}-V_{obs,i})^2}{(sd_i)^2}\right)\right), \quad (3)$$

$V_{sim,i}$ is the simulated value of the measurement, and *N* is the number of measurements. Each time-lapse survey collected in April was weighted as shown in Eqs. (2) and (3) and fit to the same χ^2 value of 0.2. The May 1 baseline inversion (Figure 8C) and May timelapse inversions were fit to a χ^2 value of 0.32.

4.0 Inversion Results

4.1 April 1 Baseline Inversion

Figure 11 shows several representations of the April 1 baseline inversion. Figure 11A shows an oblique view of the outer boundaries. The transition in BEC from low to high with depth nominally occurs at approximately 130 m in elevation and is presumably caused by the upper RLM contact at 130 m and/or the perched water table at approximately 125 m in elevation. Figure 11B-D show different representations that highlight the development of two high BEC mounds beneath the south pond. The location of the mounds should be interpreted in the context provided by the feasibility and performance simulations. Namely, the horizontal position is likely to be better resolved than the vertical position. Furthermore, the iso-surface (0.008 S/m) in Figure 11C and D was chosen to highlight the horizontal position of the peaks. The vertical positioning is less certain, and is likely higher in the section than shown in Figure 11B-D. Although these mounds could be caused by discharge water mounding on the RLM (representing a highly saturated condition), they could also be caused by natural variations in porosity or saturation. However, as the forthcoming time-lapse images will show, both mounds experienced a decrease in BEC when discharge was switched to the north pound. Such behavior is consistent with desaturation of perched water mounding on the RLM during south pond discharge.

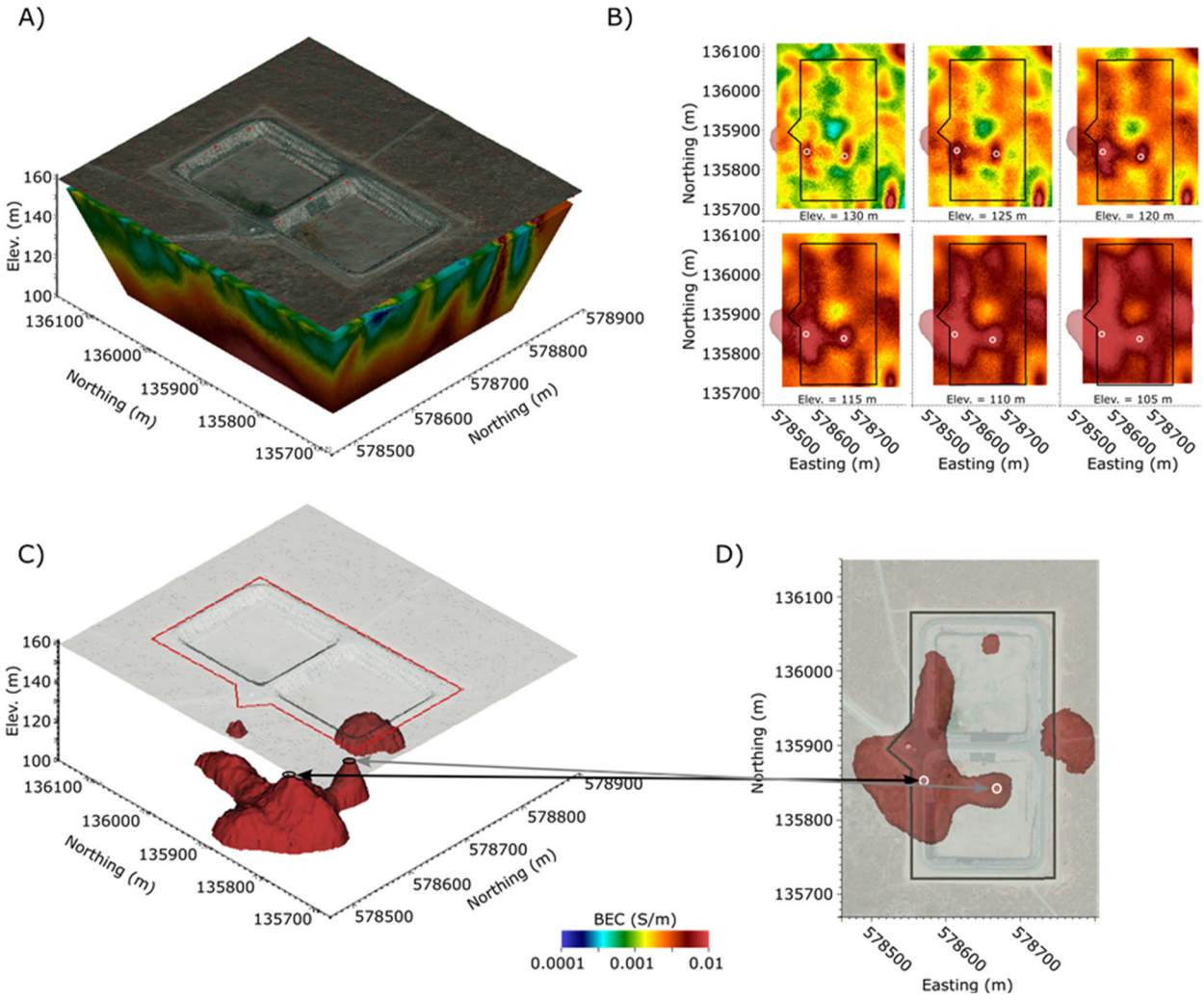

Figure 11. Four representations of April 1, 2022, baseline ERT image, taken after approximately 30 days of discharge into the south pond. A) Oblique view of image boundaries overlain by TEDF satellite image (3x vertical exaggeration). B) Horizontal slices at six depths showing development of two high-conductivity mounds with depth. C) Oblique view of 0.008 S/m iso-surface outlining high-conductivity mounds. D) Plan view of 0.008 S/m iso-surface outlining footprint of high-conductivity mounds. Open white circles in B) and D) indicate locations of mound peaks shown in C).

4.2 April Time-Lapse Difference Inversion: South Pond

Figure 12 shows the April baseline inversion (for reference) and eight time-lapse images of the change in BEC from the April 1 baseline. Beginning with vadose zone beneath the south pond, there was a decrease in BEC beginning on or before April 5 (Figure 12, 04/05 panel) in the area of the western-most anomalous mound identified in the April 1 baseline image (Figure 11). This is the expected BEC behavior for a desaturating perched water mound for two reasons. First, noting that saturation ranges between 0 and 1, the derivative of BEC with respect to saturation is largest when the soil is fully saturated [i.e., S=1, see Eq. (1)]. In other words, the change in BEC with respect to saturation is largest when the soil moves from a fully saturated to a partially saturated state. Second, under gravity draining conditions, fluid flux from a fully saturated soil will be greater than for a partially saturated soil. The combined effects are that, when the source of infiltrating water is removed, saturation will decrease more rapidly within a fully saturated

perched water mound than in the partially saturated soil above the mound, and the corresponding decrease in BEC will be larger within the perched water mound than within the unsaturated soil. This behavior is consistent with the change in BEC shown on April 5 and supports the conclusion that the decrease in conductivity beneath the south pond was caused by a desaturating perched water mound.

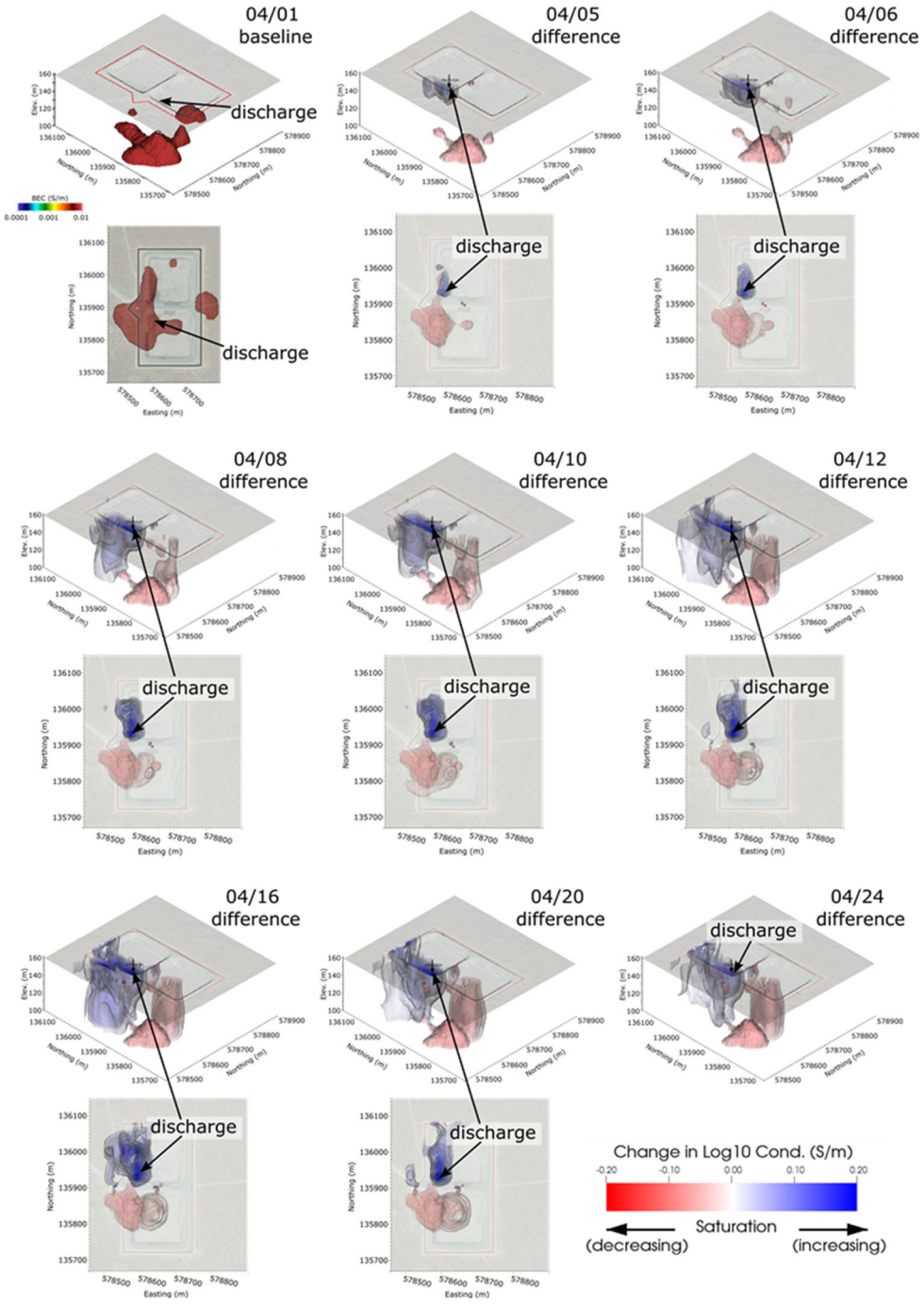

Figure 12. April time-lapse difference imaging results showing changes in BEC from April 1. Discharge switches from the south pond to the north pond between April 1 and 5. Changes show when and where the vadose zone beneath the south pond and north pond is respectively desaturating and saturating.

The decrease in BEC above the smaller, eastern-most mound identified in the baseline image exhibited similar behavior in that the BEC first decreased at the location of the mound. From April 6 to April 12, the negative BEC anomaly increased in magnitude and propagated toward the surface, *suggesting decreases in saturation that mark the primary flow paths from the pond to the RLM*. As will be shown, these flow paths are consistent with the re-saturating phase that occurred when discharge returned to the south pond in May. By April 16, decreases in BEC within the south pond reached a relative steady state, suggesting that saturation beneath the south pond reached a relative steady state approximately 15 days after south pond discharge ended.

It is notable that the soil above the larger, western-most BEC mound did not appear to desaturate over time like the soil above the eastern-most BEC mound, suggesting the western-most mound was "disconnected" from infiltrating water. Although it is possible that discharge water migrated laterally to the western mound and was undetected by the time-lapse imaging, there is little evidence to support or refute this hypothesis.

4.3 April Time-Lapse Difference Inversion: North Pond

Unlike the south pond, changes in BEC within the north pond (1) began at the surface of the pond and (2) increased rather than decreased when discharge was switched to the north pond. This was the expected behavior early on as discharge water began to infiltrate from the surface downward, thereby increasing saturation and BEC. From April 5 to April 16, the BEC anomaly grew and moved downward, *marking the primary flow paths from the surface to the RLM* in the north pond. Although the largest changes in BEC occur beneath the discharge point, the deep infiltration pathways occur further north, being centered along the western margin of the pond approximately 60 m north of the discharge point. After April 12, changes in BEC fluctuate in magnitude, likely due to corresponding changes in discharge rate (and therefore saturation), but the position of those changes remains relatively constant, suggesting flow paths through the vadose zone also remain constant.

Figure 13 shows a photograph of the north pond during infiltration. The outline of the ponding water (and the plant growth where water ponds) matches the surface expression of the increase in BEC shown in Figure 12.

Figure 13. Photograph of the western boundary of the north pond, taken from between the two ponds at approximately (175570 m east, 135900 m north), facing north. The outline of the ponded zone and plant growth (lightly colored region within in the ponded zone) match the surface expression of the change in BEC during north pond discharge (Figure 11).

4.4 May 1 Baseline Inversion

Results of the May 1 baseline inversion, collected after 30 days of discharge into the north pond (Figure 8), are shown in Figure 14. Again, the elevated BEC anomalies highlighted in Figure 14B-D likely appear lower in elevation than they are due to the limited vertical resolution in the ERT image. In contrast to the April 1 baseline shown in Figure 11, the high-conductivity anomalous BEC mounds in the south pond have largely dissipated, further suggesting that those anomalies were caused by perched water mounding during south pond discharge. Furthermore, an anomalous BEC mound has developed in the north pond that lies directly beneath the primary flow paths identified in the April time-lapse inversion results (Figure 12). These results are all consistent with the interpretation that the May 1 baseline BEC mound is caused by perched water mounding after 30 days of discharge into the north pond. In both the April 1 and May 1 baseline images, there appears a persistent, elongated anomalous BEC mounding along the western boundary of both ponds (i.e., beneath the discharge points) that extends from approximately 200 m from northing 135800 m to northing 136000 m.

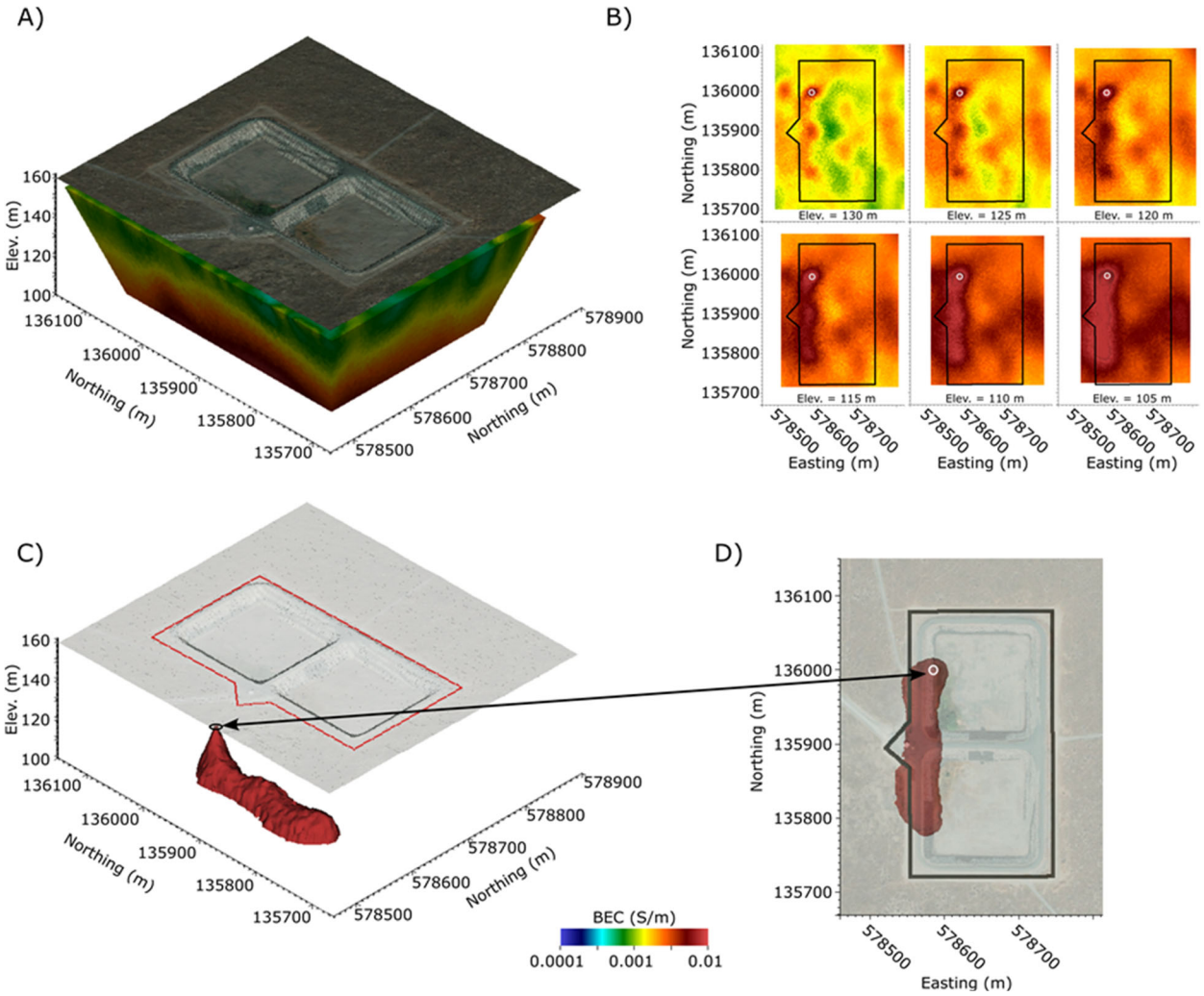

Figure 14. Four representations of May 1, 2022, baseline ERT image, taken after approximately 30 days of discharge into the north pond. A) Oblique view of image boundaries overlain by TEDF satellite image (3x vertical exaggeration). B) Horizontal slices at six depths showing development of high-conductivity mound with depth. C) Oblique view of 0.008 S/m iso-surface outlining high-conductivity mound. D) Plan view of 0.008 S/m iso-surface outlining footprint of high-conductivity mound. Open white circles in B) and D) indicate location of the BEC mound peak shown in C).

4.5 May Time-Lapse Difference Inversion: South Pond

Figure 15 shows the May 1 baseline ERT image and eight time-lapse difference images of the change in BEC from baseline. In this case, discharge was switched to the south pond after 30 days of flow into the north pond. From May 1 to 20, the BEC anomaly appears at the surface, grows, and moves downward along the primary flow paths to the RLM as discharge water infiltrates through the vadose zone. Increases in BEC appear to have stabilized by approximately May 16, with small variabilities likely caused by variable flow into the south pond. The increases in BEC that occurred during the saturation phase are consistently co-located with the decreases in BEC that occurred in the desaturation phase, as shown in Figure 12. This provides two consistent lines of evidence marking the flow paths from the south pond to the RLM. Those flow paths appear to be primarily vertical and centered near the center of the south pond at (578650 m east, 135820 m north).

Figure 16 shows a partial photograph of the south pond during discharge, including the northern boundary. The photo was taken from the western margin of the pond facing east and shows that ponded water extends farther to the east in the south pond than in the north pond, just as shown in the time-lapse ERT images. The southern extent of the ponded zone is not visible in the photograph, but also matches the increase in conductivity at the surface shown in Figure 15.

The May time-lapse imaging provides some insight into the western-most BEC mound that appeared in both the April baseline and time-lapse images and displayed BEC behavior consistent with a desaturating groundwater mound. No such mound appears to have re-formed during the May discharge into the south pond. Because of this, results and recommendations in this report focus on the discharge flow paths, which show consistent behavior when saturating and desaturating.

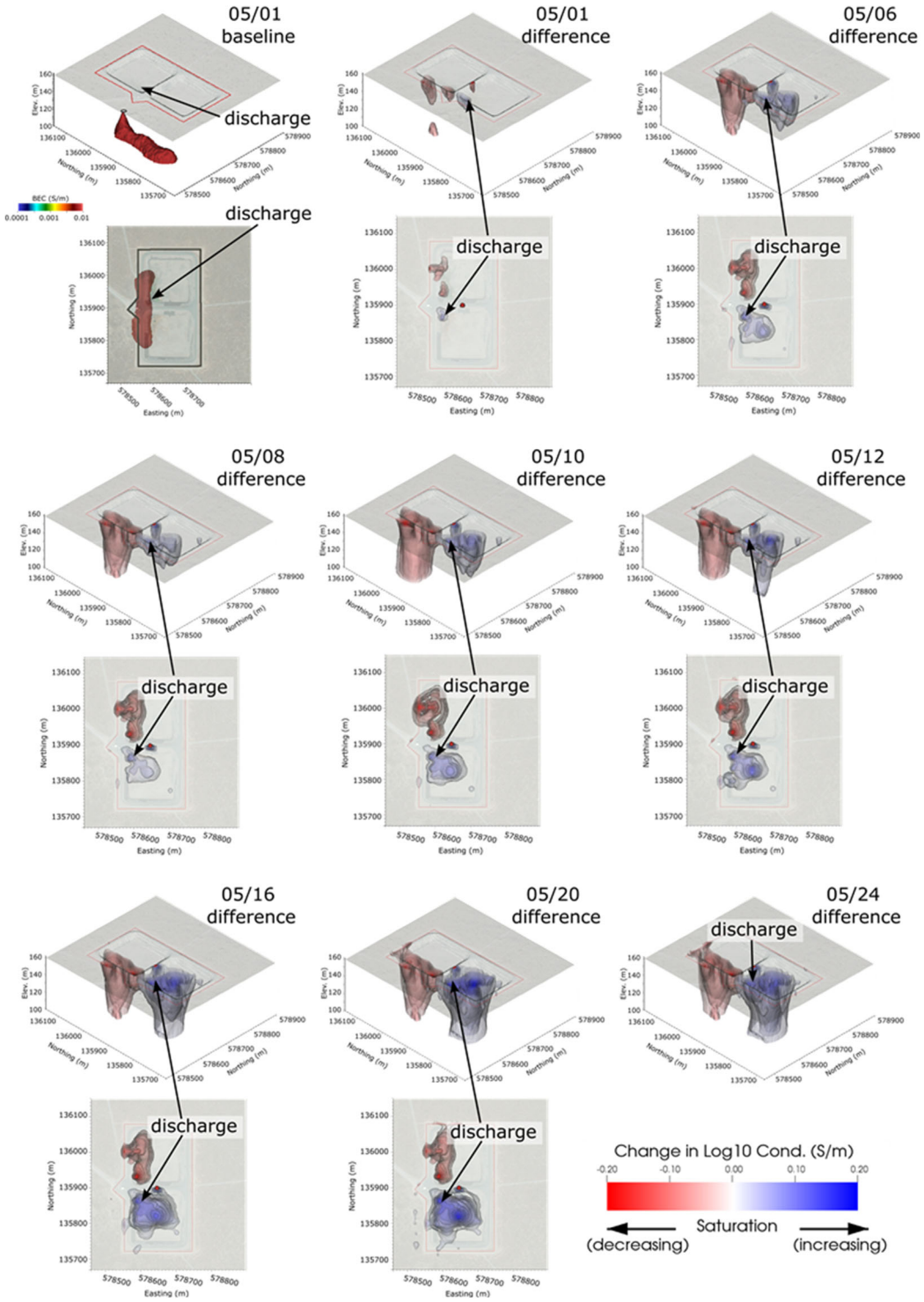

Figure 15. May time-lapse difference imaging results showing changes in BEC from May 1. Discharge switches from the north pond to the south pond between May 1 and 2. Changes show when and where the vadose zone beneath the north pond and south pond is respectively desaturating and saturating.

Figure 16. Photograph of the northern boundary of the south pond, standing between the two ponds at approximately (175570 m east, 135880 m north), facing east. The outline of the ponded zone and plant growth (lightly color region within in the ponded zone) match the surface expression of the change in BEC during north pond discharge (Figure 15).

4.6 May Time-Lapse Difference Inversion: North Pond

The vadose zone beneath the north pond experienced a period of desaturation in May, with a corresponding decrease in the BEC, as expected (Figure 15). Small decreases in BEC in both shallow and deep areas of the pond are evident on May 5. By May 6, the decrease in BEC extends from the surface to the bottom of the imaging zone. By May 12, the decrease in BEC appears to have stabilized, suggesting that decreases in saturation have also stabilized. Like the south pond, the locations of change in BEC during saturation (in April) and desaturation (in May) are consistent, and presumably mark the primary flow paths of discharge water from the north pond to the RLM. Those flow paths appear to be primarily vertical and centered at the western margin of the north pond, directly north of the discharge point at approximately (578590 m east, 136010 m north).

5.0 Summary

The primary objective of the work presented in this report is to provide information to support locating a new monitoring well screened within the presumed perched water zone that develops on the RLM unit beneath the TEDF. Representative samples of TEDF discharge water from the perched water zone are needed to understand the overall impacts on groundwater quality for TEDF permitting. Ideally, the new monitoring well will be screened where the perched water column is thickest, thereby optimizing the probability of enabling adequate samples to be collected. Presumably, the perched water column is thickest at the point(s) where the primary flow paths from the TEDF ponds enter the perched water table. Time-lapse ERT imaging was strategically used to locate the primary flow paths by identifying regions of the vadose zone that experienced the largest episodes of increasing and decreasing saturation (as indicated by corresponding changes in BEC) during corresponding of episodes of discharge to the north and south ponds.

One anomaly in the south pond exhibited the expected behavior of the perched water mound but did not appear to be directly connected to infiltration flow paths from the surface. This effect could have been caused by un-resolved lateral flow deeper in the formation. However, because the mound does not appear to re-form during flow to the south pond after April 1, the focus here is on the primary flow paths consistently imaged during discharge to both the north and south ponds. Two independent time-lapse imaging campaigns conducted during separate discharge events to the north and south ponds provided consistent results regarding changes in BEC to identify the dominant infiltration flow paths from each pond to the RLM. The flow paths appear to be primarily vertical but located away from the discharge points in each pond. In the south pond, the apparent flow paths intersect the RLM elevation near the center of the pond at approximately (578650 m east, 135820 m north). The corresponding point in the north pond occurs along the western margin of the pond boundary at approximately (578590 m east, 136010 m north).

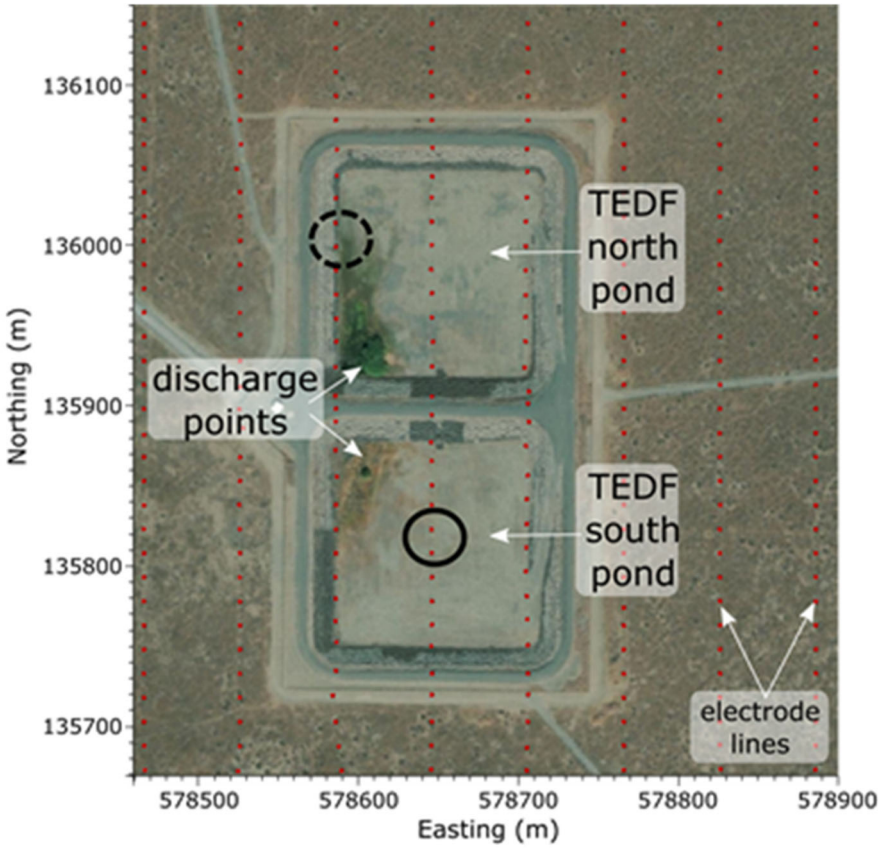

Figure 17. ERT-derived locations of dominant flux to the RLM during discharge to the north pond (dashed circle) and south pond (solid circle).

6.0 Quality Assurance

This work was performed in accordance with the Pacific Northwest National Laboratory Nuclear Quality Assurance Program (NQAP). The NQAP complies with DOE Order 414.1D, “Quality Assurance.” The NQAP uses NQA-1-2012, “Quality Assurance Requirements for Nuclear Facility Application,” as its consensus standard and NQA-1-2012 Subpart 4.2.1 as the basis for its graded approach to quality.

7.0 References

CPCC-00327, Rev. 0. 2021. Simulation of Potential Saturation Profiles at the Hanford Treated Effluent Disposal Facility (TEDF) to Support a Planned Electrical Resistivity Tomography (ERT) Study. Richland, WA: Prepared by S.S. Papadopulos & Associates, Inc., for Central Plateau Cleanup Company. https://pdw.hanford.gov/document/AR-18665

Day-Lewis, F.D., K. Singha, and A.M. Binley. 2005. "Applying petrophysical models to radar travel time and electrical resistivity tomograms: Resolution-dependent limitations." *Journal of Geophysical Research: Solid Earth* 110(B8).

DOE Order 414.1D, "Quality Assurance." Washington, D.C.: U.S. Department of Energy.

NQA-1-2012, "Quality Assurance Requirements for Nuclear Facility Application." New York, NY: American Society of Mechanical Engineers.

WRPS-1602336. 2016. Submittal of Revised 2016 State Waste Discharge Permit St0004502 Renewal Application. Richland, WA: Washington River Protection Solutions.

Pacific Northwest National Laboratory

902 Battelle Boulevard
P.O. Box 999
Richland, WA 99354

1-888-375-PNNL (7665)

www.pnnl.gov